Supplementary Information of

Generation of out-of-plane polarized spin current by non-uniform oxygen octahedral tilt/rotation

Furong Han[1†], Jing Zhang[2†], Fan Yang[3†], Bo Li[1], Yu He[1], Guansong Li[4], Youxiang Chen[1], Qisheng Jiang[2], Yan Huang[1], Hui Zhang[1], Jine Zhang[1], Huaiwen Yang[1], Huiying Liu[3], Qinghua Zhang[4], Hao Wu[2], Jingsheng Chen[5], Weisheng Zhao[1], Xian-Lei Sheng[3]*, Jirong Sun[4,6]*, Yue Zhang[1]*

[1] Fert Beijing Research Institute, National Key Lab of Spintronics, School of Integrated Circuit Science and Engineering, Beihang University, Beijing 100191, P. R. China.

[2] Songshan Lake Materials Laboratory, Dongguan, Guangdong 523808, P. R. China.

[3] School of Physics, Beihang University, Beijing 100191, P. R. China.

[4] Beijing National Laboratory for Condensed Matter Physics & Institute of Physics, Chinese Academy of Sciences, Beijing 100190, P. R. China.

[5] Department of Materials Science and Engineering, National University of Singapore, Singapore 117575, Singapore.

[6] Spintronics Institute, Jinan University, Jinan, Shandong 250022, P. R. China.

† These authors contributed equally: Furong Han, Jing Zhang, Fan Yang.

* e-mail: xlsheng@buaa.edu.cn; jrsun@iphy.ac.cn; yz@buaa.edu.cn

Section 1. Crystal quality of CRO films

The root mean square (RMS) surface roughness extracted from the atomic force microscope (AFM) image is about 0.4 nm, as shown in Fig. S1a, indicating that CRO films in this study have little surface roughness. The rocking curve of CRO films grown on LAO substrate is measured as shown in Fig. S1b, the full width at half maximum (FWHM) is about 0.03 deg and the broadening of the rocking curve is within that of substrate, indicating a good crystallinity.

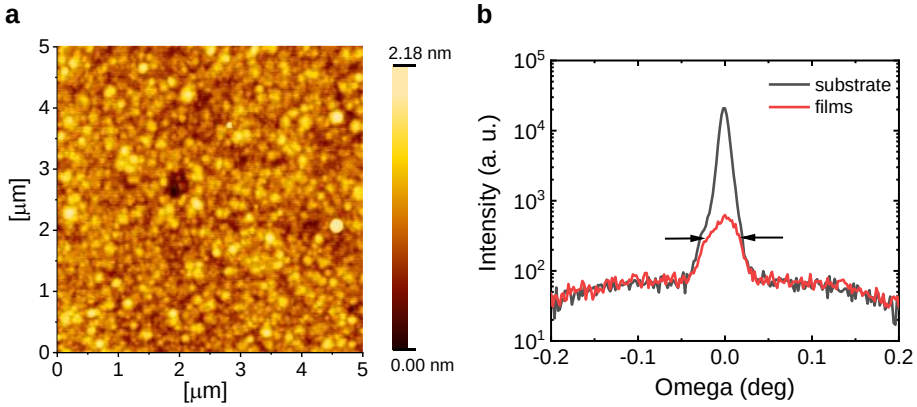

Fig. S1 a, Atomic force microscope (AFM) image of CRO films, b, Rocking curve of CRO (10 nm) films grown on LAO substrate.

Section 2. RSMs for the (103) reflections of CRO films

The reciprocal space mappings (RSMs) for the (103) reflections of CRO film are measured at different phi as shown in Fig. S2. The CRO films possess the same out-of-plane lattice constant at different phi, indicating that CRO films share a fourfold symmetry with the substrates. In theory, the CRO films with orthogonal structure should exhibit twofold symmetry, and the presence of twinned crystal domains prevents anisotropy from being visible.

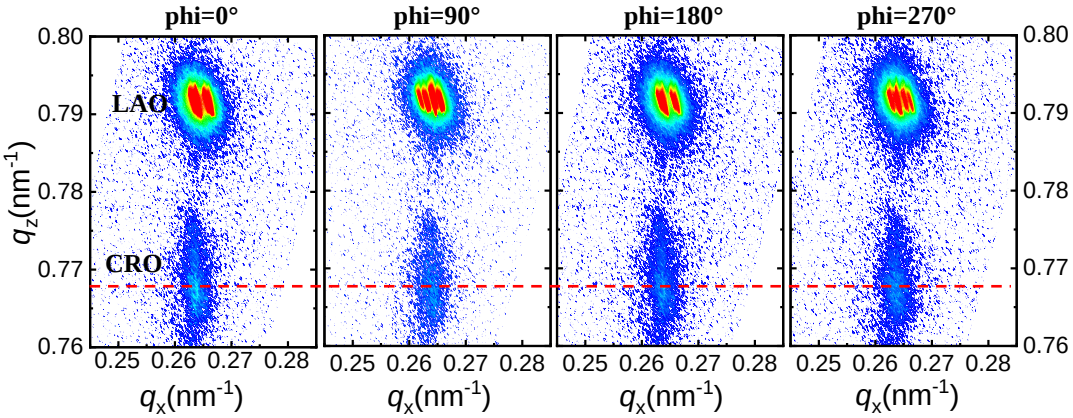

Fig. S2 Reciprocal space mappings (RSMs) for the (103) reflections of CRO film grown on LAO substrate at different phi. The red dashed line marks the peak of CRO film.

Section 3. Anisotropy of resistivity

The CRO films grown on LAO substrate are etched into devices which are along [110] and [1$\bar{1}$0]-axes, respectively, as shown in Fig. S3a. The resistivity measurements are performed and the currents are along [110] and [1$\bar{1}$0]-axes, respectively. The measurement results show that the resistivity along the [110] and [1$\bar{1}$0]-axes exhibits the same behavior and the upturn is at the same temperature as shown in Fig. S3b. The difference of resistivity between the two axes is pretty small, thus the anisotropy between the [110] and [1$\bar{1}$0]-axes is confirmed.

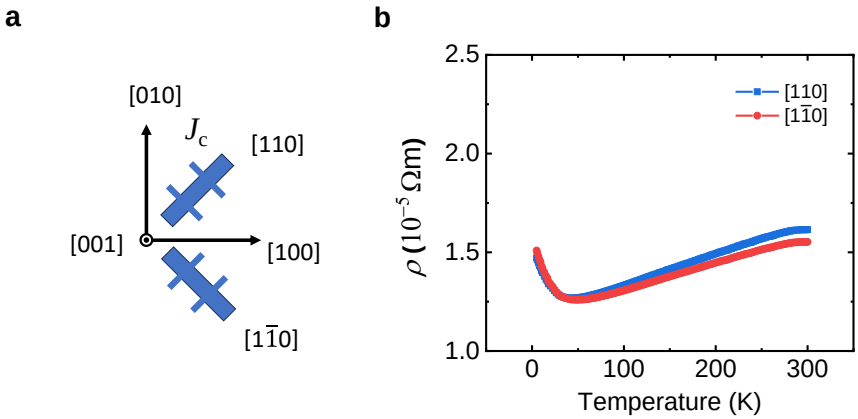

Fig. S3 a, Schematic setup of devices along [110] and [1$\bar{1}$0]-axes, respectively. b, Four-terminal resistivity as a function of temperature for CRO films along [110] and [1$\bar{1}$0]-axes, respectively.

Section 4. Crystal symmetry analyses of bulk CRO

As we have mentioned in the main text, the subscription α of the SHC element $\sigma_{\alpha\beta;\gamma}$ denotes the direction of the spin flows, β denotes the direction of the applied electric field, and γ denotes the direction of the spin polarization. The current and the electric field are polar vectors, and the spin polarization is a pseudo-vector. The pseudo-vector behaves the same as the polar vector under the constraints from proper rotation operators. But acting the inversion, mirror and improper rotation operators, on the pseudo-vector will produce an additional -1 factor. When the electric field is parallel to the *a*-axis of the orthorhombic cell, acting the inversion operator on the three SHC elements, we have

$$\sigma_{zx;x} \to \sigma_{(-z)(-x);x} = \sigma_{zx;x},$$
$$\sigma_{zx;y} \to \sigma_{(-z)(-x);y} = \sigma_{zx;y},$$
$$\sigma_{zx;z} \to \sigma_{(-z)(-x);z} = \sigma_{zx;z}.$$

So the inversion will not affect the SHC. Acting the screw axis operator $\widetilde{C_{2a}}$ on the SHC elements, we have

$$\sigma_{zx;x} \to \sigma_{(-z)x;x} = -\sigma_{zx;x},$$
$$\sigma_{zx;y} \to \sigma_{(-z)x;(-y)} = \sigma_{zx;y},$$
$$\sigma_{zx;z} \to \sigma_{(-z)x;(-z)} = \sigma_{zx;z}.$$

So the $\sigma_{zx;x}$ is enforced to be equal to $-\sigma_{zx;x}$, which means the $\sigma_{zx;x}$ element is forbidden. And the $\sigma_{zx;y}$ and $\sigma_{zx;z}$ are allowed. Acting the glide plane $\widetilde{M_a}$ on the SHC elements, we have

$$\sigma_{zx;x} \to \sigma_{z(-x);x} = -\sigma_{zx;x},$$
$$\sigma_{zx;y} \to \sigma_{z(-x);(-y)} = \sigma_{zx;y},$$
$$\sigma_{zx;z} \to \sigma_{z(-x);(-z)} = \sigma_{zx;z}.$$

The constraints from the glide plane $\widetilde{M_a}$ is the same as $\widetilde{C_{2a}}$. So following the above procedures, we can list out the Table S1, to show the existence of all the related SHC elements with the symmetries of the *Pbnm* space group. Thus, the generation of *z*-direction polarized spin current needs to break the $\widetilde{C_{2b}}, \widetilde{M_b}$ and $\widetilde{C_{2c}}, \widetilde{M_c}$ symmetry when the charge current is along the *a*-axis of the orthorhombic cell. Similarly, the generation of *z*-direction polarized spin current needs to break the $\widetilde{C_{2a}}, \widetilde{M_a}$ and $\widetilde{C_{2c}}, \widetilde{M_c}$ symmetry when the charge current is applied along the *b*-axis of the orthorhombic cell.

Symmetry Operators	SHC elements		
	$\sigma_{zx;x}$	$\sigma_{zx;y}$	$\sigma_{zx;z}$
P	○	○	○
$\widetilde{C_{2a}}, \widetilde{M_a}$	×	○	○
$\widetilde{C_{2b}}, \widetilde{M_b}$	×	○	×
$\widetilde{C_{2c}}, \widetilde{M_c}$	○	○	×

Table S1. Related SHC elements with the symmetries of the *Pbnm* space group when the charge current is along the *a*-axis of the orthorhombic cell, ○ means allowed and × means forbidden.

Section 5. Schematic of symmetry

The screw axis $\widetilde{C_{2b}}$ is broken under the non-uniform distortion, as shown in Fig. S4a, which includes the rotation symmetry C_b and translation symmetry $T_{1/2,1/2,1/2}$ along the *a*-, *c*-axes. Similar to the $\widetilde{C_{2b}}$, $\widetilde{M_b}$ is also broken, which include the translation symmetry along *c*-axis. The $\widetilde{C_{2a}}$ cannot be preserved under the structural distortion. However, the glide plane $\widetilde{M_a}$ is preserved, as illustrated in Fig. S4d, due to this symmetry relies on the mirror symmetry M_a and in-plane translation symmetry $T_{1/2,1/2,0}$. Compared to the *a*-axis, the symmetry of the *b*-axis is lower for the CRO under distortion. Due to the twinned crystal domains, both the *a*-axis and *b*-axis will grow along the [110]-axis, flattening the anisotropy between [110]- and [1$\bar{1}$0]-axes.

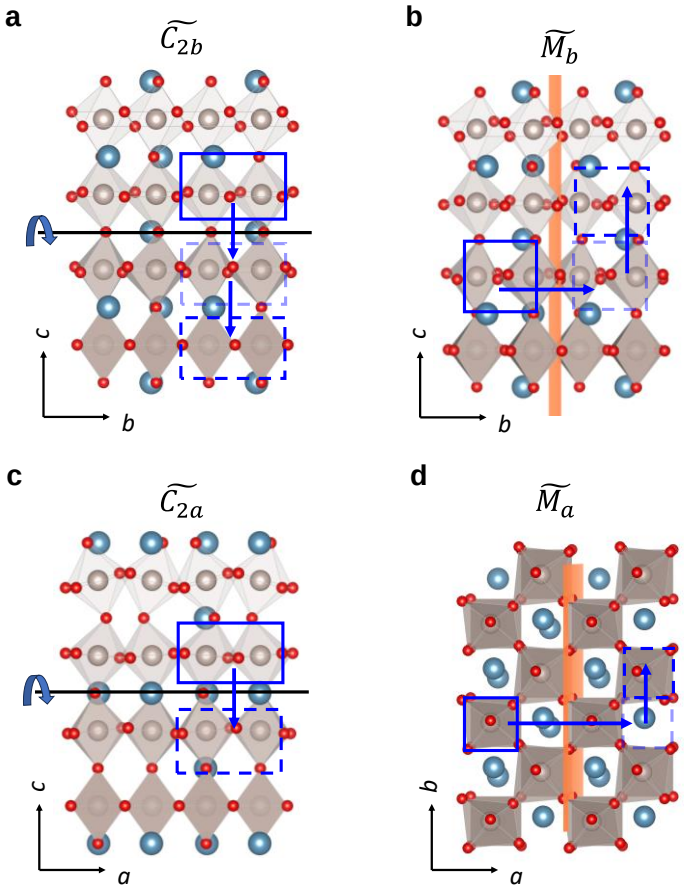

Fig. S4 a, Schematic of screw axis $\widetilde{C_{2b}}$. b, Schematic of glide plane $\widetilde{M_b}$, which includes the mirror symmetry M_b and translation symmetry $T_{1/2,1/2,1/2}$ along the *a*-, *c*-axes. The plot only shows the translation symmetry operation along the *c*-axis. The blue boxes mark the location of symmetry operation. c, Schematic of screw axis $\widetilde{C_{2a}}$. d, Schematic of glide plane $\widetilde{M_a}$, which includes the mirror symmetry M_a and translation symmetry $T_{1/2,1/2,0}$ along the *b*-axis.

Section 6. Surface states spectra and spin Berry curvature of CRO

The surface states of orthorhombic CRO at Fermi energy for the (001) and the (100) surfaces are obtained from DFT calculations, as shown in Figs. S5 a-b. The distinct features indicate that Fermi surfaces are open only in the k_z direction, which are in good agreement with the experimental results of ARPES[1].

In addition, we calculate the k-resolved distributions of the spin Berry curvature and find a correspondence with the band anisotropy. We plot the distribution of $\Omega_{zx;y}$ as an example in Figs. S5 c-d. It can be seen from the spin-Berry-curvature distributions for the (001) film that the pattern and the strength along the k_x and k_y directions are very close for different k-planes and energy levels. But for the (100) film, the pattern and the strength along k_y and k_z directions show obvious differences. The calculated spin-Berry-curvature distributions are consistent with the anisotropic electronic structure illustrated in Figs. S5 a-b.

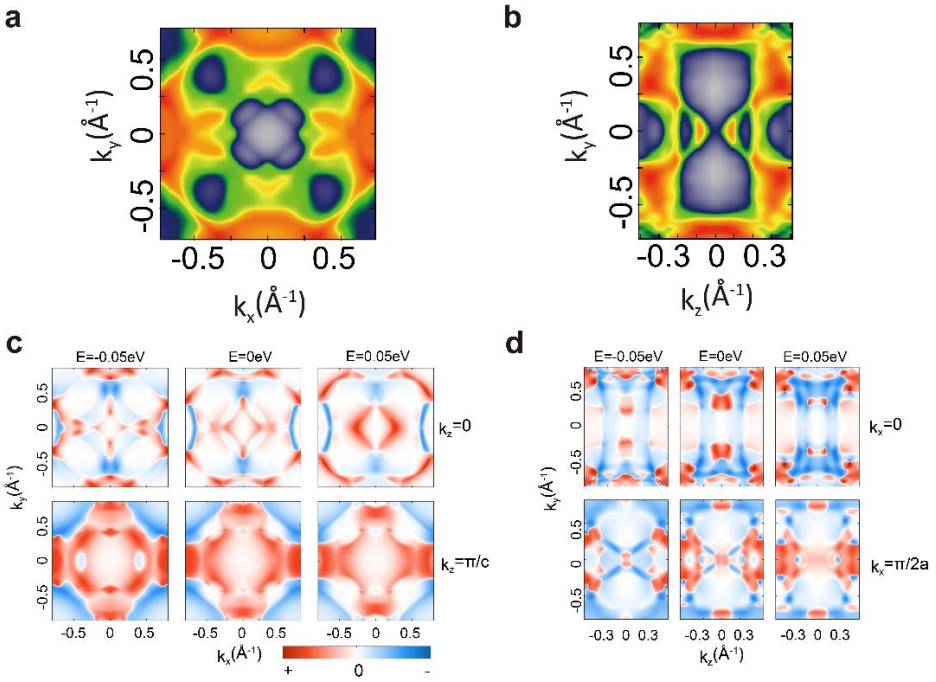

Fig. S5 a, b Surface state spectra of orthorhombic CRO at Fermi energy for the (001) (a) and the (100) surfaces (b). c, d Distributions of the spin Berry curvature $\Omega_{zx;y}$ at different energy levels (left panel: E = -0.05 eV, middle panel: E = 0 eV, right panel: E = 0.05 eV), for k_z cut (c) and k_x cut (d).

Section 7. Spin Hall conductivity of bulk CRO without distortion

For comparison, we calculate the spin Hall conductivity of bulk CRO without distortion as shown in Fig. S6. The value of $\sigma_{zx;y}$ remains on the order of ($\hbar$/2e)×10^4 $\Omega^{-1}m^{-1}$, while $\sigma_{zx;z}$ can be ignored.

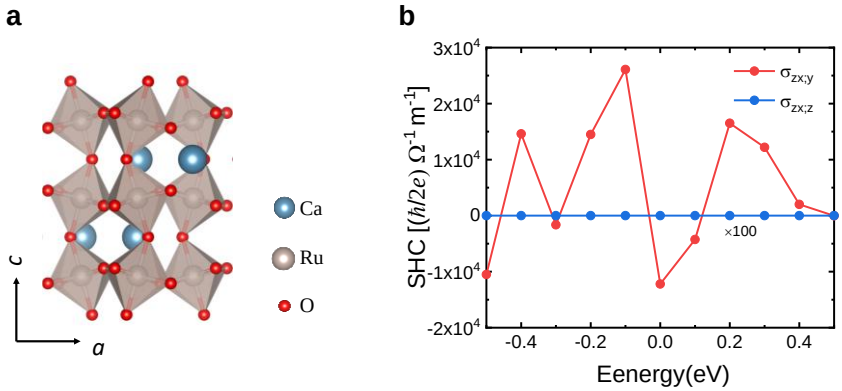

Fig. S6 a, Model of bulk CRO structure without distortion. b, Spin Hall conductivity as a function of energy of bulk CRO structure without distortion.

Section 8. Effective magnetization and Gilbert damping coefficient

By performing ST-FMR with a sequence of microwave frequencies and fitting the resonance fields to the Kittel equation: $f = (\gamma/2\pi)\ [H_0(H_0 + 4\pi M_{eff})]^{1/2}$, the effective magnetization can be determined, where γ is the gyromagnetic ratio. The effective magnetization of Py/CRO bilayers is 9.81 kOe, as shown in Fig. S7a. The Gilbert damping coefficient α is derived from the linear fitting of line width Δ versus resonant frequency f: $\Delta=\Delta_0+(2\pi\alpha/\gamma)\ f$, and the slope defines the Gilbert damping coefficient, where Δ_0 is the extrinsic contribution that is usually frequency independent, and α is 0.010 for Py/CRO bilayers as shown in Fig. S7b.

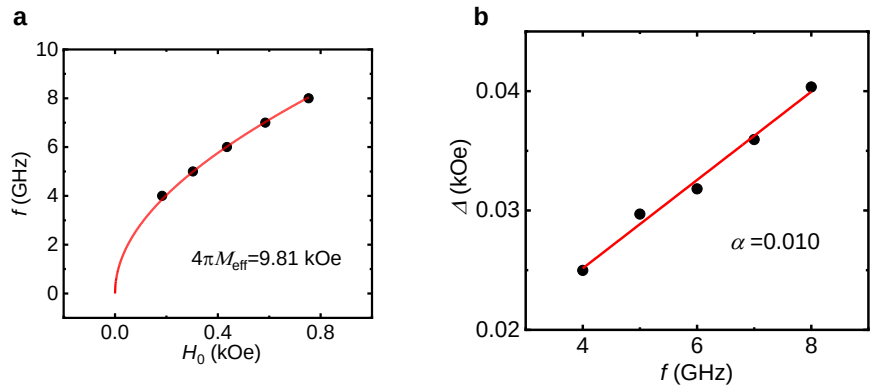

Fig. S7 a, Effective magnetization of Py (6 nm)/CRO (10 nm). b, Gilbert damping coefficient α of Py (6 nm)/CRO (10 nm).

Section 9. Resistance measurement of CRO films

The resistance as a function of temperature for CRO (10 nm) films grown on different substrates are tested by means of four-terminal as shown in Fig. S8. The CRO films grown on LAO substrate show metal conductivity and that grown on LSAT and STO substrate show semiconductor conductivity due to the strain induced by substrate.

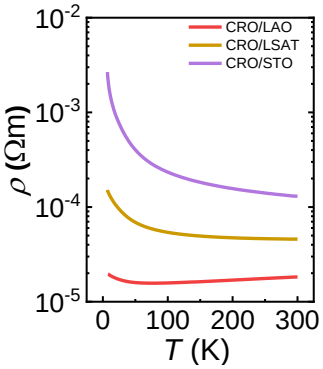

Fig. S8 Four-terminal resistance as a function of temperature for CRO films grown on different substrates.

Section 10. Contribution of Joule heating effect in SOT efficiency

The microwave-power-dependent ST-FMR signal in the CRO/Py device at 5 GHz from 9 to 19 dBm is shown in Fig. S9a. As the power increases from 9 to 16 dBm, the voltage of the symmetric component V_S in our device varies linearly, which demonstrates the magnetization precession is in the linear regime, thus eliminating the influence of thermal effect induced by microwave power. On the other hand, the V_S signal deviates from linearity at higher power (from 17 to 19 dBm), which implies Joule heating effect from higher microwave power.

The Joule heating can cause spin current between the layers, inducing additional resonant voltage signals, which exhibits a dependence on the angle of an in-plane magnetic field in the ST-FMR measurement that is identical to the signal from the SOT. We thus carry out second harmonic measurements to separate the voltages from spin current and Joule heating.

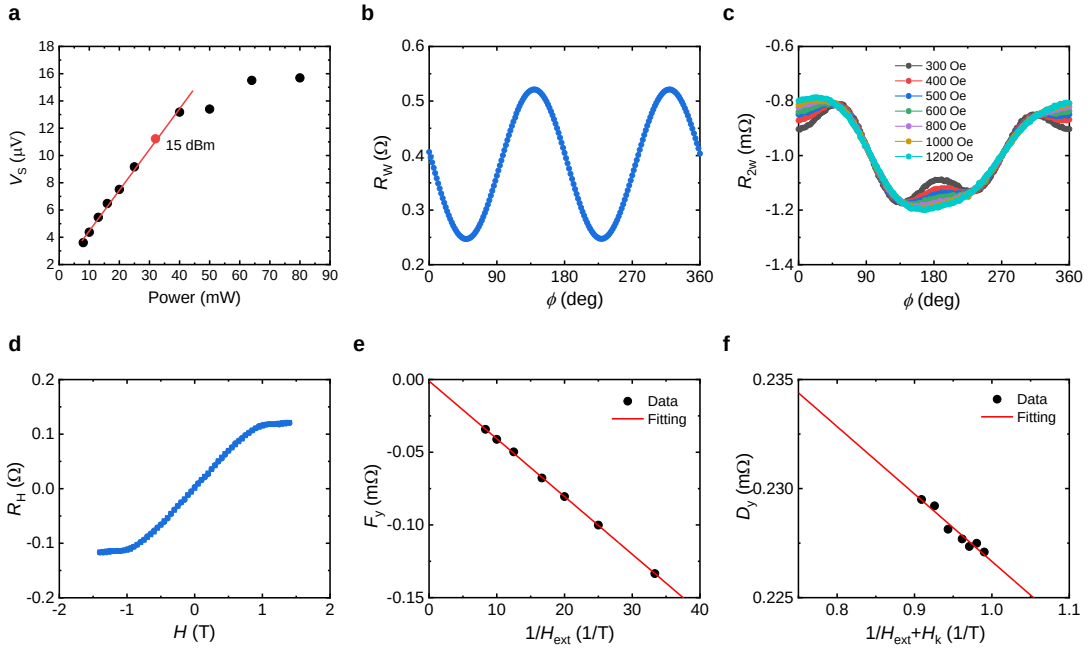

Fig. S9 a, Microwave power dependence of V_S extracted from the ST-FMR signals. b, First harmonic Hall resistance (R_ω) as a function of in-plane rotation angle ϕ. c, Second harmonic Hall resistance ($R_{2\omega}$) as a function of in-plane rotation angle ϕ, under different external magnetic field. d, Perpendicular magnetic field dependence of the Hall resistance (R_H). e-f, Linear plot of F_y against $1/H_{ext}$ (e) and D_y against $1/H_{ext}+H_k$ (f).

The Py/CRO heterostructure is patterned into Hall bars with a width of 20 um. An ac current with frequency of 1.33 KHz was injected into the Hall bar, the current densities in CRO films is 2.57×10^5A/cm^2. The first (R_w) and second (R_{2w}) harmonic Hall voltages were measured using lock-in as a function of the external magnetic field angle as show in Figs. S9b and S9c, respectively. The SOT torque can be separated from the in-plane rotation angle ϕ dependence voltage signals using following equation:

$$R_{2w} = F_y(2cos^3\phi - cos\phi) + D_y cos\phi + R_{ther} sin2\phi$$

with

$$F_y = 2R_{PHE}\frac{H_y^{FL}+H_O}{H_{ext}}$$

$$D_y = R_{AHE}\frac{H_y^{DL}}{H_{ext}-H_K} + R_{ANE}$$

Where D_y term consists of the contributions from both the damping-like torque coefficients generated by the spin Hall effect and the anomalous Nernst effect (R_{ANE}); F_y term is the superposition of field-like torque and Oersted field counterparts (y represents the direction of polarization). The R_{ther} term has been removed during data processing, which is likely to arise from a thermal gradient along the direction of current. The H_y^{DL} is y-polarized damping-like torque effective fields. The H_y^{FL} and H_O are y-polarized field-like torque effective fields and Oersted field, respectively. R_{AHE} is the coefficient of the peak anomalous Hall voltage as shown in Fig. S9d. R_{PHE} is the coefficient of the peak planar Hall effect voltage for the given amplitude of alternating current as shown in Fig. S9b. H_{ext} is external magnetic field and H_K characterizes the magnetic anisotropy. The F_y against $\frac{1}{H_{ext}}$ is plotted to extract the $H_y^{FL}+H_O$ from the gradient of the linear fit as shown in Fig. S9e. The $H_y^{FL}+H_O$ derived from linear fitting is 0.145 Oe showing that field-like torque effective fields are pretty small. The D_y against $\frac{1}{H_{ext}-H_K}$ is plotted to extract the H_y^{DL} from the gradient of the linear fit as shown in Fig. S9f. The good linear relation for the D_y against $\frac{1}{H_{ext}-H_K}$ is the direct evidence of a sizable damping-like torque. The torque efficiencies per unit electric field associated are:

$$\xi_{y,z}^{DL}=\frac{2eH_{y,z}^{DL}m_s}{\hbar J}$$

where J is the current density in the CRO layer, m_s is the saturation magnetization of the Py layer. We find ξ_y^{DL}=1.2 at room temperature which is close to the efficiency from ST-FMR measurements. Thus, the SOT from spin Hall effect is dominant and Joule heating only contributes a small portion.

Section 11. Comparison of charge-spin interconversion with 4*d*/5*d* transition oxides

The second harmonic measurement is performed as shown in Fig. S9. The damping-like torque effective magnetic field is proportional to the slope of the linear plot of D_y against $1/H_{ext}+H_k$ and estimated to be 10.5 Oe/(10^{10} Am^{-2}). It can be found in Table S2 that, due to the strong spin-orbit coupling, 4*d*/5*d* transition oxides usually have a high efficiency for charge-spin interconversion. By comparing the effective magnetic field and SOT efficiency, we can see that the CRO films provide one of the largest efficiencies of charge-spin interconversion among 4*d*/5*d* transition oxides.

Table S2. Comparison of the effective magnetic field from second harmonic measurement and SOT efficiency from ST-FMR measurement of 4*d*/5*d* transition metal oxides from recent works.

Year	Author	Heterostructures	thickness	effective field (/10^{10} Am^{-2})	SOT efficiency ($\hbar$/2e)	Temperature
this work	Han, F. *et al.*	$CaRuO_3$/Py	10 nm	10.5 Oe	1.4	300 K
2023[2]	Li, S. *et al.*	$SrRuO_3$/Py $SrRuO_3$/CoPt	20 nm	1.38 Oe (θ=0.18) 3.96 Oe (θ=0.21)	—	300 k
2023[3]	Li, P. *et al.*	$SrIrO_3$/CoFeB	10.8 nm	3.57 Oe	1.4	300 K
2019[4]	Nan, T. *et al.*	$SrIrO_3$/Py	20 nm	—	0.58	300 K
2019[5]	Liu, L. *et al.*	$SrRuO_3$/$SrIrO_3$	8 nm	—	0.86	70 K
2019[6]	Everhardt, A. S. *et al.*	$SrIrO_3$/Py	13 nm	—	0.33	300 K
2019[7]	Wang, H. *et al.*	$SrIrO_3$/$Co_{1-x}Tb_x$	30 nm	—	1.1	300 K
2019[8]	Ou, Y. *et al.*	$SrRuO_3$/Co	10 nm	—	0.1 (300 K) 0.23 (60 K)	60-300 K
2016[9]	Wahler, M. *et al.*	$SrRuO_3$/$La_{0.7}Sr_{0.3}MnO_3$	1.2 nm	—	0.027	190 K
2021[10]	Wei, J. *et al.*	$SrRuO_3$/Py	6 nm	—	0.04-0.89	300 K
2021[11]	Zhou, J. *et al.*	$SrRuO_3$/Py	20 nm	—	0.015-0.15	300 K
2020[12]	Bose, A. *et al.*	IrO_2/Ir/Py	5 nm	—	0.65 (30 K) 0.08 (300 K)	30-300 K
2020[13]	Ueda, K. *et al.*	IrO_2/Py	7 nm	—	0.09	300 K

Section 12. Magnetism of CRO films

Zero-field-cooled (ZFC) and field-cooled (FC) magnetization curves taken after cooling the sample without applying a magnetic field and while cooling the sample in an applied magnetic field with 1000 Oe are measured as shown in Fig. S10a, respectively. The increase of magnetization with the decrease of temperature comes from the LAO substrate. The curves of magnetization versus field (*M-H*) are measured at the temperature varied from 10 to 300 K as shown in Fig. S10b.

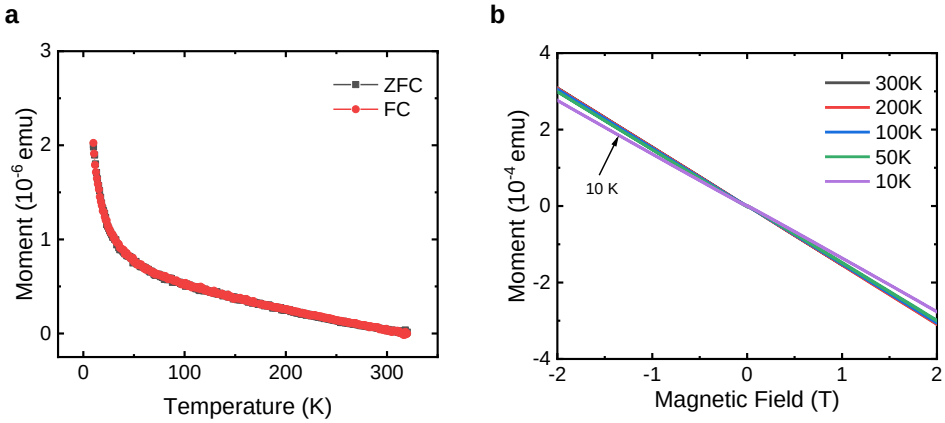

Fig. S10 a, Zero-field-cooled (ZFC) and field-cooled (FC) magnetization versus temperature for CRO (10 nm) films grown on LAO substrate. b, Magnetic-field dependence of magnetization for CRO films measured at different temperatures.

Section 13. ST-FMR measurement of CRO films with thickness of 25 nm

The antisymmetric component V_A can be well fitted using the conventional torque terms cosφsin2φ (τ_y^{FL} components) as shown in Fig. S11, thus the z-direction polarized SOT is pretty small and can be ignored.

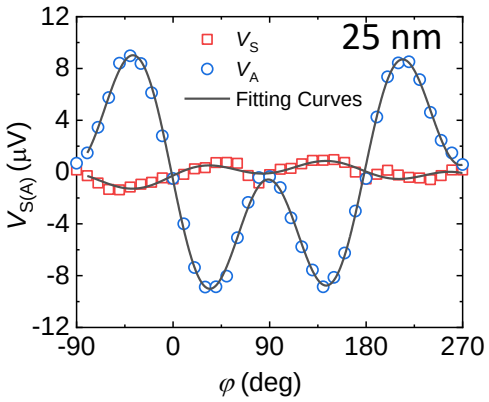

Fig. S11 Angular dependence of V_s and V_a of the Py (6 nm)/CRO (25 nm) bilayers and fitted by cosφsin2φ.

Section 14. In-plane anisotropy measurements

Fig. S12 shows the ST-FMR measurement when the measurement device is rotated of 90°. The *z*-direction SOT can be observed when the charge current is applied along [110] or [1$\bar{1}$0]-axis, which is consistent with the fourfold symmetry of the CRO films. Due to the twinned crystal domains, both the *a*-axis and *b*-axis of orthorhombic structure will grow along the [110]-axis of cubic substrate, destroying the anisotropy between [110]- and [1$\bar{1}$0]-axes. The twinned crystal domains of orthogonal structures produced on a cubic substrate flatten the in-plane anisotropy of SOT in measurement, even though it exists intrinsically.

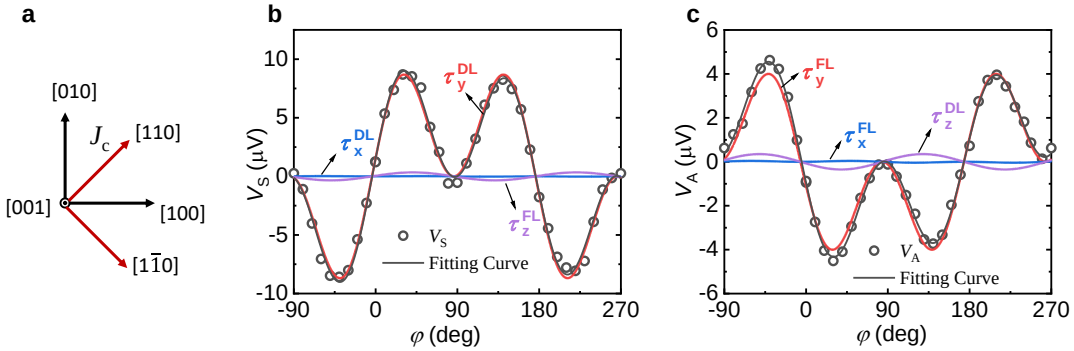

Fig. S12. a, Schematic setup of in-plane anisotropy measurements. The coordinate system is based on the pseudo-cubic structure of the CRO film. The Py/CRO device is along the [110]-axis b-c, Symmetric and antisymmetric voltage amplitudes depending on applied field angle for Py/CRO device. Black circles indicate the extracted values from ST-FMR measurement. The red, blue, and purple curves represent the calculations of τ_x, τ_y, and τ_z, respectively, from the analyses using Eqs. (1) and (2).

Section 15. ST-FMR measurement of CRO films grown on different substrate

The lattice mismatch between bulk CRO and substrate varies from −1.53% on LAO, +0.47% on $(LaAlO_3)_{0.3}(SrAl_{0.5}Ta_{0.5}O_3)_{0.7}$ (LSAT) to +1.41% on $SrTiO_3$ (STO) ("−" denotes compressive strain, "+" denotes tensile strain). Because of the strain applied in CRO, the CRO lattices can be stretched or compressed, which alters the tilt and rotation angle of the RuO_6 octahedra. Figs. S13a-b display the HAADF image and ABF image of CRO/STO, which confirm the high crystal quality. According to the analysis of STEM image, the Ru-O-Ru bond angle in the atomic layer relaxes gradually and finally gets a value of ~176°. The relaxation length scale for the oxygen octahedral tilt/rotation is about 8 unit cells as shown in the left panel of Fig. S13c. The displacement x_O of the O anion along the [001]-axis direction gradually increases and saturates as the CRO layer shifts away from the CRO/STO interface as shown in the right panel of Fig. S13c. Compared to the CRO films on LAO substrate, the oxygen octahedral tilt/rotation of CRO films on STO substrate is suppressed by the tensile strain and the relaxation length scale is reduced, which is consistent with the reported result. Thus, the thickness of CRO films with non-uniform structural modification is reduced.

The SHC of the Py/CRO bilayers grown on LSAT and STO substrate can be obtained from the angular dependence of ST-FMR signals shown in Fig. S14a and S14b, respectively. From Fig. S14c, we can find that the SHC of *y*-direction polarized spin current tuned by strain has different trends, which can be attributed to the band structure of CRO influenced by the octahedral crystal field. The SHC of *z*-direction polarized spin current shows obvious dependance on strain and decreases when the strain changes from compressive to tensile strain, as demonstrated in Fig. S14d. This trend is consistently with the change of crystal structure under different strain, which further confirm that the generation of *z*-direction SOT is dependent on the modification of structure.

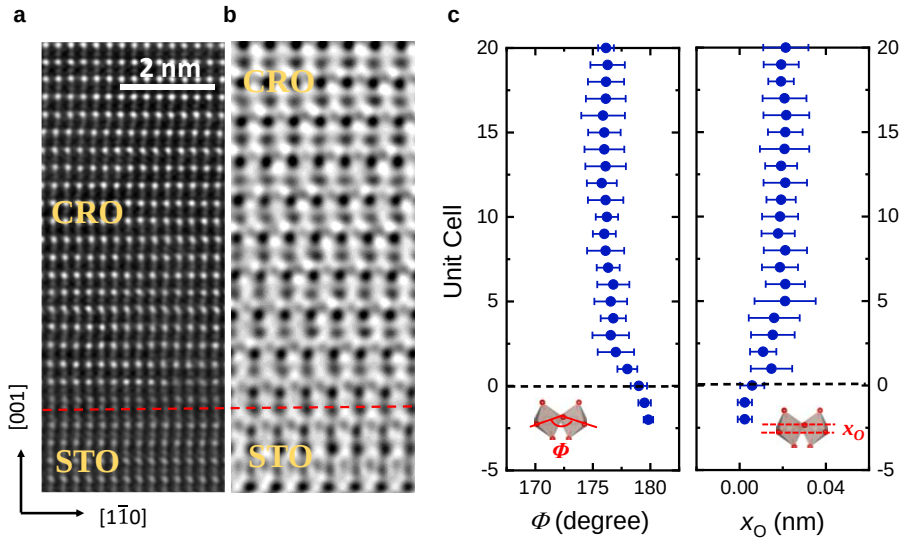

Fig. S13 Crystal structure of CRO films grown on STO substrate. a, HAADF image of the cross section of CRO/STO, recorded along the [110] zone axis. The interfaces are marked by red dashed line, showing clearly layered structures and atomically sharp interface. b, ABF image of CRO/STO, the interface is marked by red dashed line. c, Averaged Ru-O-Ru bond angle Φ (left) and displacements of O anion x_O (right) plotted as a function of the pseudo-cubic CRO layer. The error bars denote the standard deviation of multiple measurements. The Ru-O-Ru band angle Φ and the displacements of O anion x_O are sketched in the inset plots.

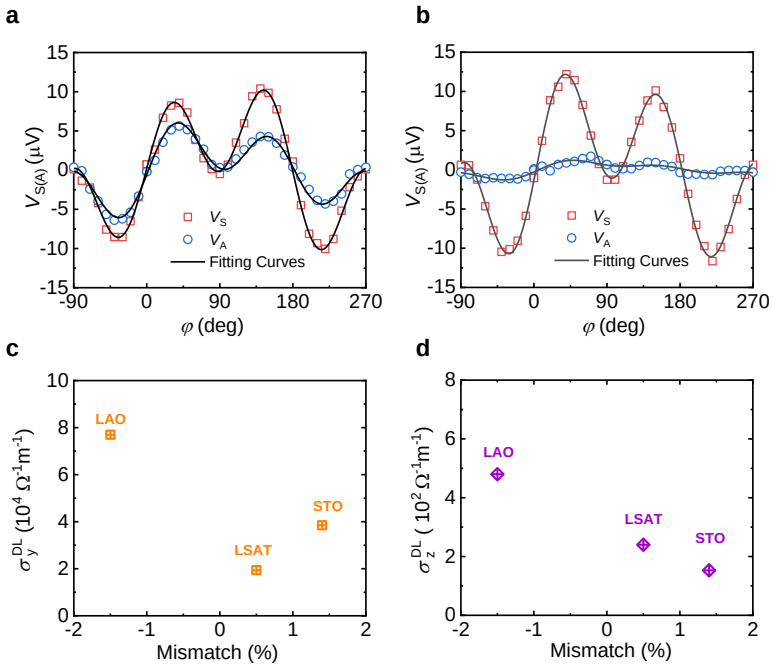

Fig. S14 a-b, Angular dependence of V_s and V_a of the Py/CRO bilayers grown on LSAT (a) and STO (b)substrate. The black lines are the fitting curves by using the Eqs. (1) and (2). c-d, SHC of *y*- (c) *z*-direction polarized spin current dependance on mismatch between bulk CRO and substrate.

Section 16. Anomalous Hall loops of Hall bar device

The anomalous Hall loop is measured at 300 K, which confirms the perpendicular magnetic anisotropy (PMA) of the CoFeB layer.

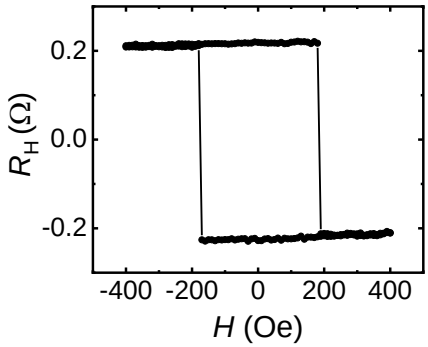

Fig. S15 Anomalous Hall loops of Hall bar device at 300 K.

Section 17. Comparison with other field-free systems

The critical current densities for field-free switching in different heterostructures are summarized in Table S3. The CoFeB/CRO system requires lower current density than most of heterostructures. Although the critical current density in $SrRuO_3/SrIrO_3$ heterostructure is smaller than that in CoFeB/CRO heterostructure, the working temperature of $SrRuO_3/SrIrO_3$ heterostructure is below room temperature. The comparison with other field-free systems indicates the high efficiency of field-free perpendicular magnetization switching in CoFeB/CRO system.

Table S3. Summary of critical current density for field-free switching in different heterostructures.

Year	Author	Heterostructures	Critical current density ($\times 10^{10} Am^{-2}$)	Temperature
this work	Han, F. *et al.*	$CaRuO_3$/CoFeB	6.3	300 K
2019[3]	Liu, L. *et al.*	$SrRuO_3/SrIrO_3$	4.6	70 K
2022[14]	Kao, IH. *et al.*	$WTe_2/Fe_{2.78}GeTe_2$	9.8	190 K
2023[15]	Liu, Y. *et al.*	$TaIrTe_4$/CoFeB	7.6	300 K
2021[16]	You, Y. *et al.*	$Mn_3SnN/(Co/Pd)_3$	9	300 K
2023[17]	DC, M. *et al.*	$MnPd_3$/Co	11	300 K
2021[18]	Chen, X. *et al.*	$Mn_2Au/(Co/Pd)_3$	55	300 K
2022[19]	Karube, S. *et al.*	RuO_2/Co	30	300 K
2021[20]	Zheng, Z. *et al.*	$Co_{1-a}Tb_a$	9	300 K
2016[21]	Oh, YW. *et al.*	IrMn/CoFeB	42	300 K
2016[22]	Lau, YC. *et al.*	Pt/CoFe/Ru /CoFe/IrMn	20	300 K

Section 18. Shunting effect analysis in Hall bar device

For the Ta (2 nm)/MgO (2 nm)/CoFeB ($Co_{20}Fe_{60}B_{20}$, 1.2 nm)/Ti (3 nm)/CRO (9 nm) device shown in Fig. 4, the critical current is 9 mA. The resistivities of CRO (9 nm) and the PMA structure CoFeB (1.2 nm)/Ti (3 nm) layers (the Ta layer will be oxidized in air), can be obtained from standard four-probe measurements. We have the resistivity for each layer $\rho_{CRO} = 1.1\times10^{-5}\ \Omega\cdot m$ and $\rho_{PMA} = 4.7\times10^{-6}\ \Omega\cdot m$. The width of CRO layers is 16 μm and the PMA layers are etched into round pillar with a diameter of 10 μm.

The resistivity of round pillar PMA layers can be calculated as:

$$R_{PMA} = \int_{-r}^{r} \frac{\rho_{PMA} dl}{s} = \frac{\pi \rho_{PMA}}{2t_{PMA}}$$

The critical current density by considering the parallel circuit model can be estimated as:

$$\begin{aligned} I_{CRO} &= I_{all} \frac{R_{PMA}}{R_{CRO} + R_{PMA}} \\ &= I_{all} \frac{\frac{\pi \rho_{PMA}}{2t_{PMA}}}{\frac{\rho_{CRO} l_{CRO}}{w_{CRO} \times t_{CRO}} + \frac{\pi \rho_{PMA}}{2t_{PMA}}} \\ &= 9\ mA \times \frac{\frac{\pi \times 4.7 \times 10^{-6}\ \Omega \cdot \mathrm{m}}{2 \times 4.2\ nm}}{\frac{1.1 \times 10^{-5}\ \Omega \cdot \mathrm{m} \times 10\mu\mathrm{m}}{16\ um \times 9\ nm} + \frac{\pi \times 4.7 \times 10^{-6}\ \Omega \cdot \mathrm{m}}{2 \times 4.2\ nm}} \\ &= 6.3\ mA \end{aligned}$$

$$\begin{aligned} J_{CRO} &= I_{CRO} \times \frac{1}{w_{CRO} \times t_{CRO}} \\ &= 6.3\ mA \times \frac{1}{16\ um \times 9\ nm} \\ &= 4.4 \times 10^{10}\ \mathrm{A}m^{-2} \end{aligned}$$

Therefore, thirty percent portion of the current flows into the PMA structure. The contribution of current induced torque from the Ti layer is negligible due to the extremely small spin Hall angle of Ti. The critical current density for the field-free switching is as low as $4.4\times10^{10}\mathrm{A}m^{-2}$, when considering the shunt effect.

Section 19. Joule heating effect analysis for SOT switching measurement

When the current flows through the Hall bar, a temperature rise is likely to be generated due to the Joule heating effect. Therefore, it is necessary to calibrate the instant device temperature at the switching point. We measured the resistance of device as a function of temperature, for which a tiny dc current 10 μA is applied to avoid heating effect. As shown in Fig. S16a, a linear dependence is obtained. Then, we measured the exact resistance when applying pulsed current as shown in Fig. S16b. The pulsed current with density of 6.3×10^{10}Am^{-2} gives a resistance of 1150 Ω, and the instant device temperature is determined to be 354 K.

The impact of temperature rise on the PMA layer is further analyzed. The anomalous Hall resistance curves versus out-of-plane magnetic field under different temperatures are measured as shown in Fig. S16c. We can see that the CoFeB ferromagnetic layer is below the Curie temperature and maintains perpendicularly ferromagnetic when the pulsed current is applied.

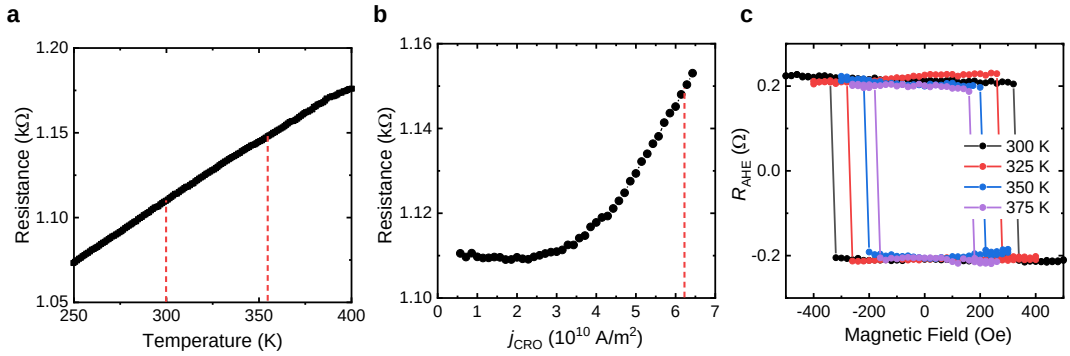

Fig. S16 a, Resistance of device as a function of temperature. b, Resistance of device as a function of the pulsed current density. c, Anomalous Hall resistance curves versus out-of-plane magnetic field under different temperatures.

References

1. Liu, Y. *et al.* Revealing the hidden heavy Fermi liquid in $CaRuO_3$. *Phys. Rev. B* ***98***, 041110, (2018).
2. Li, S. *et al.* Room temperature spin-orbit torque efficiency and magnetization switching in $SrRuO_3$-based heterostructures. *Phys. Rev. Mater.* **7**, 024418 (2023).
3. Li, P. *et al.* Large Spin-Orbit-Torque Efficiency and Room-Temperature Magnetization Switching in $SrIrO_3$/Co-Fe-B Heterostructures. *Phys. Rev. Appl.* 19, 024076 (2023).
4. Nan, T. *et al.* Anisotropic spin-orbit torque generation in epitaxial $SrIrO_3$ by symmetry design. *Proc. Natl. Acad. Sci. U.S.A.* **116**, 16186-16191 (2019).
5. Liu, L. *et al.* Current-induced magnetization switching in all-oxide heterostructures. *Nat. Nanotechnol.***14**, 939-944 (2019).
6. Everhardt, A. S. *et al.* Tunable charge to spin conversion in strontium iridate thin films. *Phys. Rev. Mater.* **3**, 051201 (2019).
7. Wang, H. *et al.* Large spin-orbit torque observed in epitaxial $SrIrO_3$ thin films. *Appl. Phys. Lett.* **114**, 232406 (2019).
8. Ou, Y. *et al.* Exceptionally High, Strongly Temperature Dependent, Spin Hall Conductivity of

$SrRuO_3$. *Nano Lett.* **19**, 3663–3670 (2019).
9. Wahler, M. *et al.* Inverse spin Hall effect in a complex ferromagnetic oxide heterostructure. *Sci. Rep.* **6**, 28727 (2016).
10. Wei, J. *et al.* Enhancement of Spin-Orbit Torque by Strain Engineering in $SrRuO_3$ Films. *Adv. Funct. Mater.* 31, 21000 (2021).
11. Zhou, J. *et al.* Modulation of Spin-Orbit Torque from $SrRuO_3$ by Epitaxial-Strain-Induced Octahedral Rotation. *Adv. Mater.* 33, 2007114 (2021).
12. Bose, A. *et al.* Effects of Anisotropic Strain on Spin–Orbit Torque Produced by the Dirac Nodal Line Semimetal IrO_2. *ACS Appl. Mater. Interfaces* 12, 55411–55416 (2020).
13. Ueda, K. *et al.* Spin-orbit torque generation in NiFe/IrO_2 bilayers. Phys. Rev. B 102(13), 134432 (2020).
14. Kao, IH. *et al.* Deterministic switching of a perpendicularly polarized magnet using unconventional spin-orbit torques in WTe_2. *Nat. Mater.* **21**, 1029–1034 (2022).
15. Liu, Y. *et al.* Field-free switching of perpendicular magnetization at room temperature using out-of-plane spins from $TaIrTe_4$. *Nat. Electron.* **6**, 732–738 (2023).
16. You, Y. *et al.* Cluster magnetic octupole induced out-of-plane spin polarization in antiperovskite antiferromagnet. *Nat. Commun.* **12**, 6524 (2021).
17. DC, M. *et al.* Observation of anti-damping spin-orbit torques generated by in-plane and out-of-plane spin polarizations in $MnPd_3$. *Nat. Mater.* **22**, 591–598 (2023).
18. Chen, X. *et al.* Observation of the antiferromagnetic spin Hall effect. *Nat. Mater.* **20**, 800–804 (2021).
19. Karube, S. *et al.* Observation of Spin-Splitter Torque in Collinear Antiferromagnetic RuO_2. *Phys. Rev. Lett.* **129**, 137201(2022).
20. Zheng, Z. *et al.* Field-free spin-orbit torque-induced switching of perpendicular magnetization in a ferrimagnetic layer with a vertical composition gradient. *Nat. Commun.* **12**, 4555 (2021).
21. Oh, YW. *et al.* Field-free switching of perpendicular magnetization through spin-orbit torque in antiferromagnet/ferromagnet/oxide structures. *Nat. Nanotech.* **11**, 878–884 (2016).
22. Lau, YC. *et al.* Spin-orbit torque switching without an external field using interlayer exchange coupling. *Nat. Nanotech.* **11**, 758–762 (2016).